Wear 364-365 (2016) 184–192

Contents lists available at ScienceDirect

Wear

journal homepage: www.elsevier.com/locate/wear

Semi-analytical and numerical analysis of sliding asperity interaction for power-law hardening materials

Bin Zhao [a], Song Zhang [a,*], Leon M. Keer [b]

[a] Key Laboratory of High Efficiency and Clean Mechanical Manufacture (Ministry of Education), School of Mechanical Engineering, Shandong University, Jinan, Shandong 250061, PR China
[b] Department of Mechanical Engineering, Northwestern University, Evanston, IL 60208, USA

ARTICLE INFO

Article history:
Received 9 February 2016
Received in revised form
6 July 2016
Accepted 18 July 2016
Available online 22 July 2016

Keywords:
Sliding
Asperity contact
Power-law hardening materials
Semi-analytical model
Numerical model

ABSTRACT

The study of the sliding process between asperities on rough surfaces can improve the understanding of wear mechanisms. The sliding interaction between asperities is analyzed in this paper using both a semi-analytical model and a finite element model. Power-law hardening materials are considered, and the asperity profiles are assumed to be a parabolic approximation to the cylinder. The effects of strain hardening exponents on some contact parameters are explored with the finite element model. Results show that the faster semi-analytical model agrees well with the finite element model for materials with larger hardening exponents, while for materials with smaller exponents, the errors would preclude its use. As the exponent decreases, the dragging effect in sliding becomes more notable and influences the contact parameters more significantly. Friction shows a significant effect in the sliding process after preliminary consideration, which should be explored in detail further.

1. Introduction

Sliding is present in many engineering applications where there are moving surfaces and plays an important role in mechanical behavior, such as friction and wear [1–9]. As is well-known, engineering surfaces are rough at the microscopic scale, containing distributions of asperities. When relative motion occurs between two surfaces, the asperities will interact with each other, and a fundamental issue is the mechanical effects of sliding asperity interaction.

Previous research in the literature has focused on asperity interaction. Normal contact is reviewed first. Hertz [10] considered contact between elastic, frictionless solids. Later, Greenwood and Williamson [11] advanced Hertz theory and gave a statistical description of surface parameters to study the normal contact between rough surfaces; research by others followed [12,13]. Kogut and Etsion [14] developed a finite element (FE) model to study the elastic–plastic contact between a rigid flat and a hemisphere under frictionless condition and gave dimensionless expressions for the contact parameters. Jackson and Green [15] improved upon the FE model with finer meshes, and explored the effects of geometry and material on hardness. These two FE models focused on the loading process. Etsion et al. [16] developed another FE model to consider also the unloading process of an elastic–plastic loaded spherical contact and gave equations for the residual interference after complete unloading. Later, Zhao et al. [17] studied the frictionless contact of a power-law hardening elastic–plastic sphere with a rigid flat. They explored the effects of the strain hardening exponents on the contact parameters during the loading and unloading processes. The residual interferences after complete unloading at different strain hardening exponents were also given.

In addition to the above models concentrating on the normal contact between asperities, other investigations studied sliding asperity interaction. Hamilton and Goodman [18] studied circular sliding contact and gave analytical expressions and graphs of the yield parameter and tensile stress distribution. Hamilton [19] then presented improved equations for the stresses beneath a sliding, normally loaded Hertzian contact. Tangena and Wijnhoven [20] first gave a two-dimensional (2D) FE model to describe the interaction between an elastic–plastic asperity and a rigid asperity, which moved through the soft asperity. Faulkner and Arnell [21] developed the first three-dimensional (3D) FE model to simulate the sliding interaction between elastoplastic hemispherical asperities. With this model, they obtained the normal and shear forces during the sliding. Vijaywargiya and Green [22] gave a thorough investigation of the forces, deformations, stress and energy loss during the sliding process between two elastic–plastic cylinders with the FE method. Jackson et al. [23] used a more rapid semi-analytical method to study the line-hardening elastic–plastic

* Corresponding author. Fax: +86 531 88392746.
E-mail address: zhangsong@sdu.edu.cn (S. Zhang).

http://dx.doi.org/10.1016/j.wear.2016.07.010
0043-1648/

Nomenclature

A	Contact area
A_c	Critical contact area of asperity summit
$A_c(r)$	Critical contact area at the contact point
A_{Hertz}	Hertzian contact area
C	Critical yield stress coefficient
E_1, E_2	Young's moduli of two asperities 1 and 2
E'	Combined Young's moduli
F	Asperity contact force
F_1, F_2	Contact force of asperity 1 and 2
F_c	Critical contact force of asperity summit
$F_c(r)$	Critical contact force at the contact point
F_{Hertz}	Hertzian contact force
F_n	Normal component of the contact force
F_t	Tangential component of the contact force
i	A arbitrary sliding step number
j	Total number of sliding step
k	Empirical factor in semi-analytical model
n	Hardening exponent
R	Radius of summit of asperity
R_1, R_2	Radii of summits of asperities 1 and 2
R_s	Sum of asperity summit radii
$R(r)_1$, $R(r)_2$	Radii at the contact point of asperities 1 and 2
$R_v(r)$	Equivalent radius at the contact point
r	Horizontal position of the upper asperity
S_y	Yield strength
U	Energy loss in the sliding process
U_c	Critical elastic energy
w	Interference
w_1, w_2	Interference of asperities 1 and 2
w_c	Critical interference of asperity summit
$w_c(r)$	Critical interference at the contact point
w_{res}	Residual interference
w_y	Interference defined by Greenwood and Tripp [12]
y	Maximum vertical deformation on the profile of asperity 1
α	Contact angle between two asperities
δ	Overlap of the two asperities
ν_1, ν_2	Poisson ratio of asperities 1 and 2

asperity sliding process. They treated sliding as a process having many loading and unloading stages by using the empirical expressions of contact parameters given in the above normal contact models [12–14]. Additionally, they developed a FE model to formulate empirical expressions for the tangential and normal forces in sliding interaction, and compared them with the semi-analytical model. Results showed that these two models could match well for some but not all cases. Mulvihill et al. [24] developed a FE model for the interaction of an elastic–plastic asperity junction based on cylindrical or spherical asperities. They considered large overlaps, interface shear strength and material failure and derived a means for the prediction of friction coefficients. Dawkins and Neu [25] developed a crystal plasticity finite element model to consider the influence of the crystal orientation in the sliding process. It suggested that the plastic strain and stress fields obtained by crystal plasticity are considerably different with those given by conventional isotropic $J2$ plasticity. This is an interesting study, and the crystal plasticity will be considered in the future. However, in this work, the continuum plasticity will still be used like some previous works [22,23]. Fleck et al. [26] gave the strain gradient theory of rate independent plasticity, however, many similar finite element models developed in [14–17] considered the metal materials (e.g. steel, copper etc.) without the strain-gradient approach, where the grain sizes of the materials were just like those in this work. Those models were verified by the in-situ and real-time optical experimental investigations [27,28]. Therefore, it might not be necessary to consider the strain-gradient approach at the current scale, and for the current grain sizes, though the strain-gradient approach might be a useful method.

From the literature survey, it is clear that considerable research about sliding asperity interactions has been conducted. However, in most of the models, the elastic–plastic materials of the asperities were assumed as linear hardening materials with a tangent modulus of about 2% of the Young's modulus, and therefore the power-law hardening materials requires additional investigation. In addition, the shapes of the asperities were usually treated as a sphere in 3D or a cylinder in 2D. While as suggested by [29,30], the parabola might be a more realistic profile of the asperity in 2D at least in some cases. It is because (1) the parabola could at least reflect the characteristic that the radii at the contact point could not be identical in the contact process, which might be a slight improvement; and (2) the asperity profile could be fitted with different kinds of parabola, which might be more feasible to catch the realistic profiles. Therefore, the sliding process between the asperities having parabolic profiles will be studied for power-law hardening materials, using a semi-analytical method and a FE model. The effect of strain hardening exponents on the contact parameters will be explored, including the vertical deformation, stress, contact area, contact forces and the energy loss in the sliding process. The deformation of the nodes on the surface can reveal how the asperity deforms with the tangential forces, and the stress contour can reveal the stress distribution and evolution, which can predict the appearance of wear. Also, the single tangential loading process in this work is the foundation of the reciprocating sliding related to wear due to the fatigue, or the sliding process for two surfaces. Thus this work might give some useful results for the wear community especially for someone who focuses on the power-law hardening materials.

The assumptions used here are as follows:

(1) Sliding is assumed to be frictionless. The frictionless condition omits the friction which really exists between the asperities, and thus only the effect of plasticity on the sliding are considered. This assumption might be not realistic, however, it can isolate the effect of plasticity. In addition, some friction cases are also considered with the FE model, and are compared with the cases under frictionless condition to explore the effect of the friction.
(2) The effect of the deformation of the bulk on regions close to the contact is not considered;
(3) Sliding is simulated as a quasi-static process;
(4) Temperature effects on the sliding process are ignored.

2. Semi-analytical model

From results of previous research under frictionless condition [15,16,31,32], Jackson et al. [23] developed a semi-analytical model for spherical asperity interaction, regarding the sliding process as a many loading-unloading process. As suggested in [23], the simplified unloading-loading process could simulate the sliding process to some extent, though the actual process is more complex. The semi-analytical model here follows their method with some improvement. Power-law hardening materials are considered, and

Please cite this article as: B. Zhao, et al., Semi-analytical and numerical analysis of sliding asperity interaction for power-law hardening materials, Wear (2016), http://dx.doi.org/10.1016/j.wear.2016.07.010

the profiles of the asperities are assumed as parabolas. The power-law materials can extend the material scope for the sliding process, and the parabola geometry can extend the range of the asperity shape. First, the contact force in the loading process of a loading-unloading process is calculated on the initial parabolic geometry, and the interference for each asperity is obtained; then the unloading process in the loading-unloading process is considered and the residual interference for each asperity is derived; finally, considering the effect of the residual interference on the parabolic profile (actually the radius of the asperity at the contact point), the contact force in the next loading step is computed. The process is given in detail as follows.

The elastic–plastic power-law hardening material is introduced first, where the plastic behavior obeys the J_2 flow theory and satisfies a power hardening law reconstructed by the Ramberg–Osgood curve [33]. The relation of the strain ε to the stress σ for power-law hardening materials is given as:

$$\sigma = \begin{cases} E\varepsilon, \sigma \le Sy \\ Sy((E/Sy)\varepsilon)^n, \sigma > Sy \end{cases} \tag{1}$$

where S_y and E are the yield strength and Young's modulus, and n is a strain hardening exponent varying from 0 to 1. A larger n means the material is more elastic, while the smaller n means the material is more plastic. For the two extreme cases, $n=1$ is the purely elastic case, while $n=0$ is the elastic-perfectly plastic case. Some realistic n-values for common engineering materials were given as follows [34]: for AlZn6CuMgZr (ISO) aluminum alloy, $n=0.21$; and for 18CrMo4 (ISO) steel, $n=0.15$.

Two asperities in sliding whose profiles are approximated as parabolas are shown in Fig. 1. The difference in contact between the parabola asperities and the spherical asperities is as follows: for the contact between parabola asperities, the radii of the asperity at the contact point change all the time in the sliding process; while for the contact between spherical asperities, the radii of the asperity at the contact point are identical. The upper asperity 1 slides frictionless across the lower asperity 2, whose base is fixed during the entire sliding process. Several parameters are given as follows: δ is the overlap of the two asperities; α is the contact angle; r is the horizontal position of the upper asperity, and $r=0$ is the position of the axis of symmetry for the lower asperity; F is the contact force and F_n, F_t are its normal and tangential components, whose expressions are given as:

$$\begin{cases} F_n = F\ \cos\ \alpha \\ F_t = F\ \sin\ \alpha \end{cases}. \tag{2}$$

R_1 and R_2 are the radii of the summits of asperity 1 and 2, while $R(r)_1$ and $R(r)_2$ are the radii at the contact point. The relation for R and $R(r)$ is given as the following expression [35]:

$$R(r) = R\left(1 + r^2/R_s^2\right)^{3/2}. \tag{3}$$

The interferences in different directions are given by w, w_y, while w_1, w_2 represent the actual deformations of asperity 1 and asperity 2. The expressions of w, w_y and α can be obtained by the geometric relationship [35]:

$$w = w_y\ \cos\ \alpha \tag{4}$$

$$w_y = \delta - r^2/2R_s \tag{5}$$

$$\cos\ \alpha = \left(1 + r^2/R_s^2\right)^{-0.5} \tag{6}$$

where $R_s = R_1 + R_2$ is the sum of the radii of the summits.

As assumed earlier, the sliding is treated as a quasi-static process, where the continuous sliding process is divided into many static steps. Here, the total number of steps can be assumed as j, while i represents the number of an arbitrary step in the "sliding" process. When asperity 1 "slides" across asperity 2 from the step i to $i+1$, the process can be considered as an unloading process from the step i and a subsequent loading process to the step $i+1$. Some existing loading and unloading models for power-law hardening materials are adopted as given below.

The loading process for power-law hardening materials was studied by Zhao et al. [17], and the following dimensionless expressions of the contact force F and contact area A were obtained:

$$F/Fc = \begin{cases} (w/wc)^{1.5}, & \text{for } 0 \le w/wc \le 1 \\ b_1(w/wc)^{b_2}, & \text{for } 1 \le w/wc \le 6 \\ b_3(w/wc)^{b_4}, & \text{for } 6 \le w/wc \le 110 \end{cases} \tag{7}$$

$$A/Ac = \begin{cases} w/wc, & \text{for } 0 \le w/wc \le 1 \\ c_1(w/wc)^{c_2}, & \text{for } 1 \le w/wc \le 6 \\ c_3(w/wc)^{c_4}, & \text{for } 6 \le w/wc \le 110 \end{cases} \tag{8}$$

where b_1, b_2, b_3, b_4 and c_1, c_2, c_3, c_4 are functions of strain hardening exponent n obtained by fitting the finite element results,

$$\begin{cases} b_1 = -0.07598n + 0.96081 \\ b_2 = 0.10725n + 1.43352 \\ b_3 = -0.82815n + 1.68998 \\ b_4 = 0.31831n + 1.21111 \\ c_1 = -0.01763n + 1.13173 \\ c_2 = -0.04715n + 1.03997 \\ c_3 = 0.23235n + 0.94066 \\ c_4 = -0.18325n + 1.14559 \end{cases} \tag{9}$$

The expressions of the critical interference w_c, contact force F_c and contact area A_c were adopted as given by Jackson and Green [15], and were revised since the radii at the contact point should be considered as the actual contact radii.

$$w_c(r) = \left(\pi C S_y/2E'\right)^2 Rv(r) \tag{10}$$

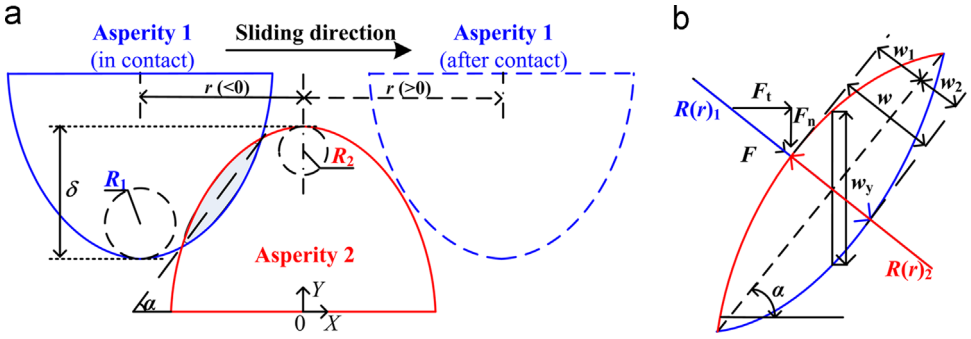

Fig. 1. Schematic of sliding asperity interaction. (a) The asperities in sliding. (b) The contact region showing interferences in different directions.

Please cite this article as: B. Zhao, et al., Semi-analytical and numerical analysis of sliding asperity interaction for power-law hardening materials, Wear (2016), http://dx.doi.org/10.1016/j.wear.2016.07.010

$$Fc(r) = 4E'Rv(r)^{1/2}w_c(r)^{3/2}/3 \tag{11}$$

$$Ac(r) = \pi^3(CS_yRv(r)/2E')^2 \tag{12}$$

where C is related to the Poisson's ratio ν of the softer material, by $C=1.295\exp(0.736\nu)$, and E' is the combined Young's modulus for the two contact surfaces:

$$1/E' = (1-\nu_1^2)/E_1 + (1-\nu_2^2)/E_2 \tag{13}$$

Here E_1, E_2 and ν_1, ν_2 are Young's moduli and Poisson ratios of two contact asperities respectively. The equivalent contact radius at the contact point is $R_v(r)$, which is given as the following expression [35]:

$$Rv(r) = \frac{R(r)_1R(r)_2}{R(r)_1+R(r)_2}. \tag{14}$$

Considering that the values of the contact forces of asperity 1 and 2 (i.e. F_1 and F_2) are the same, only the upper asperity 1 was studied, and its contact force and area were calculated with Eqs. (7) and (8). Thus the interference w in Eqs. (7) and (8) should be replaced by the interference of asperity 1, w_1 (see Fig. 1), which can be derived from the relation:

$$\begin{cases} w1+w2 = w \\ F1 = F2 \end{cases} \tag{15}$$

And the expression of w_1 can be obtained as:

$$w_1 = w\left\{1+\left[(F_c(r)_2/F_c(r)_1)^t(w_c(r)_1/w_c(r)_2)\right]^{-1}\right\} \tag{16}$$

where t is related to the functions b_2 and b_4,

$$t = \begin{cases} 2/3, & 0 < w \le 1 \\ 1/b_2, & 1 < w \le 6 \\ 1/b_4, & 6 < w \le 110 \end{cases}. \tag{17}$$

When the asperity slides from step i to step $i+1$, the asperity is unloaded from the current step i with some elastic rebound and can not return to the original shape. The residual interferences w_{res} were given by Zhao et al. [17]:

$$w_{res}/w = \left(1-1/(w/w_c)^e\right)^2 \tag{18}$$

where e is a function of n, which can be expressed as:

$$e = -0.22471n^2 - 0.17406n + 0.39877 \tag{19}$$

The residual deformation changes the geometric characteristics of the asperity, and affects the contact radii at the next step $i+1$, as revealed by Jackson et al. [23]:

$$R(r)_{i+1} = R(r)_i - k\max\left[w_{\text{res}}\right]_{0\to i} \tag{20}$$

Here, $R(r)_i$ and $R(r)_{i+1}$ are the contact radii at step i and $i+1$ respectively. k is an empirical factor related to the material property including the hardening exponent n, representing the amount of residual deformation and its affect on the contact radii at the next step, and its values are determined by fitting the finite element results.

To compare results with the numerical model later, the profiles of the asperities are approximated as two arbitrary parabolas obeying the following equations:

$$y/R = \begin{cases} (x+0.3R)^2/(2R) - \delta/R, & \text{upper asperity } 1 \\ -x^2/(2R), & \text{lower asperity } 2 \end{cases}. \tag{21}$$

The radii at the summit, R, are 50 μm for each of the two asperities. In addition, the ratio of Young's modulus to yield stress (S_y), E/S_y was set as 500, since it has negligible effect on contact parameters [36], and the Poisson's ratio ν was set to 0.3. The strain hardening exponent n ranged from 0.1 to 0.9, and the asperity overlaps ranged from $\delta=0.001R$ to $\delta=0.007R$. The range of asperity overlaps is determined due to two considerations: (1) the computational time is up to 14 hours for one case under the current overlap. When the overlap increases, the computational time will increase quite a lot; (2) The semi-analytical model only effective only for the cases $w_1 < 110w_c$, which is limited by previous expressions shown in Eqs. (7) and (8). Under the current overlap, the semi-analytical was roughly in the effective range, e.g. $w_1=46.2w_c$ at $\delta=0.001R$. For larger overlaps, the semi-analytical model might not effective. The sliding process of the asperities having the given shapes and material properties was studied. The calculations were done by Matlab 2015a for less than 3 s on a PC with 3.00 GHz processor and 16 GB of RAM. The results will be shown in detail later.

3. Numerical model

A two-dimensional plane strain FE model was developed using the software ANSYS 16.1, as shown in Fig. 2. Two asperities were assumed as the shapes given in Eq. (21), with a tangential offset r in the X direction and an asperity overlap δ in the Y direction. The zone close to the contact was of most interest and an extremely fine mesh was used to capture the curvature of the asperity and to detect the contact area radius accurately, while the zone far away from the contact had a coarser mesh. The asperities were meshed by eight-node PLANE 183 elements. The 2D three-node surface-to-surface contact element (CONTA172) and nonflexible two-node target element (TAEGET169) were used to simulate the contact between the asperities. The model consisted of 139,323 nodes and 46,033 elements including 45,737 of PLANE 183 and 146 of CONTA172 elements.

A piecewise linear/power hardening was set in ANSYS to take into account the elastic–plastic material property. The Young's modulus (E), yield stress (σ_y), and Poisson's ratio (ν) were set as the values given in Section 2. The von Mises yield criterion was employed to describe the transition from elastic to plastic deformation, and a frictionless condition was used in the contact. The boundary conditions are as shown in Fig. 2: (1) Nodes at the base of the lower asperity were restricted in all directions; (2) Nodes at the base of the upper asperity were constrained to move in the Y direction, but were allowed to move freely in the X direction. The displacement in the X direction was applied to the nodes at the base of the upper asperity step by step to simulate the sliding process, which saved some computational cost. This treatment has been verified in some previous works (e.g. [22,37]), considering the contact and sliding process. The vertical deformation, stress, contact area, contact force and energy loss were calculated and recorded at each step. The computational time ranged from 0.5 h to 14 h for different cases on a PC with 3.00 GHz processor and

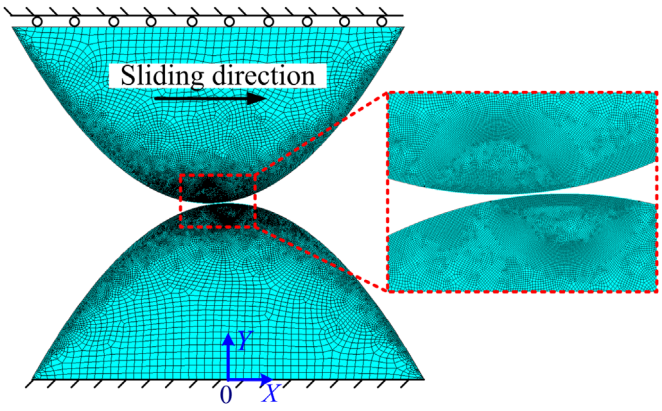

Fig. 2. Finite element model.

Please cite this article as: B. Zhao, et al., Semi-analytical and numerical analysis of sliding asperity interaction for power-law hardening materials, Wear (2016), http://dx.doi.org/10.1016/j.wear.2016.07.010

16 GB of RAM, which was much longer than that of the semi-analytical model.

To ensure the convergence and accuracy of the mesh, the mesh density was doubled iteratively and the automated meshing technique in ANSYS was changed, while the results changed no more than 1.4%, which showed the meshing was reliable. Furthermore, to verify the validity of the FE modeling method, the contact between two purely elastic asperities which were aligned vertically with respect to the axes of symmetry without sliding was studied, and the contact parameters were compared with the Hertz results [10]. The errors of the contact force and contact area were less than 2.1%. Also, the sliding process between spherical asperities for elastic-perfectly plastic materials described in the previous research [23] was studied by building an FE model with the similar method in this work. By comparison, the errors of contact forces were less than 3.7%. These verifications suggest the FE model is reliable.

4. Results and discussions

The following results are obtained in the sliding between asperities, whose hardening exponents n changes from 0.1 to 0.9 at a range of asperity overlaps δ from $0.001R$ to $0.007R$.

To compare the FE results with the semi-analytical results, Figs. 3–5 show the normal force, tangential force and contact area at some selected cases where $n=0.1$, 0.5 and 0.9 at the asperity overlap $\delta=0.001R$. The contact force is computed from the reaction forces of the nodes at the bottom of the upper asperity, and the contact force is computed from the reaction forces of the nodes at the bottom of the upper asperity, and the contact area is calculated by summing the area components of all contact elements directly by the command in ANSYS. The empirical factor $k=2$ was used in the semi-analytical model as a best fit the FE results for all the current cases (different n) as shown in Figs. 3–5. What should be noted is that the values of k are based on the finite element results in this work, and if the finite element solutions are not available, it will be difficult to determine the parameter k. Actually, the authors expect finding the empirical expressions of k for materials with different n and under different normal preloads. However, it might be much more difficult than expectation, which might be considered further in the future. The semi-analytical model is effective only for the cases $w_1 < 110w_c$, as revealed in Eqs. (7) and (8). After verification, the maximum interference w_1 is about $46.2w_c$ at $\delta=0.001R$, and the semi-analytical model appears appropriate to be used. The normal force F_n and the tangential force F_t were normlized to the Hertz contact force F_{Hertz}, which was obtained in the contact between two purely elastic asperities aligning vertically without sliding at $\delta=0.001R$, and the contact area A was also normalized to the Hertz contact area A_{Hertz}. It can been seen from Figs. 3–5 that the shapes and trends of the semi-analytical results are very similar to those of FE results for both the contact forces and contact area. When the exponents n is closer to 1.0 (e.g. $n=0.9$), the difference between the semi-analytical and FE results are smaller. The maximum errors of the normal force, tangential force and contact area are 6.07%, 11.8% and 8.1% respectively in the case $n=0.9$, while they increase much more to 31.2%, 40.5% and 27.3% in the case $n=0.1$. In addition to the small errors in developing the FE model, more errors may arise from the simplification in the semi-analytical model that the plastic deformation is considered as residual displacement. For materials with smaller n, the plastic deformation will be larger, where the simplification plays a more important role in the semi-analytical results and explains the larger errors for the materials with lower n.

The semi-analytical model is many orders of magnitude faster than the FE model. However, from the comparison above, it seems to be more appropriate for materials with higher exponents n, and while not so accurate for materials with very low exponents. Another limitation of the semi-analytical model is that it is applicable only for $w_1 < 110w_c$. Thus the FE method might be a better way to study the effect of hardening exponents on the sliding contact parameters at larger overlaps later. However, the semi-analytical model gives some helpful insights that the sliding process could be explored from empirical expressions. A more improved analytical model still needs to be developed by considering the effect of the plastic deformation for power-law hardening materials with low n.

Next the contact parameters were studied using the FE model, including the maximum vertical deformation, contact stress, contact area, normal and tangential forces, and energy loss in the sliding process for materials with differing hardening exponents n ranging from 0.1 to 0.9 as asperity overlap δ changed from $0.001R$ to $0.007R$.

Since the two asperities have the same material properties, the deformation in these two asperities is identical. The maximum vertical deformation in the Y direction, y, of the nodes on the profile of the upper asperity were recorded at each sliding step. The normalized values at the asperity overlaps $\delta=0.007R$ are shown in Fig. 6. As expected, the deformation increases with the increase of the sliding displacement until it reaches its maximum values. The maximum values of y take place after the upper asperity passes the symmetry axis ($r=0$) because of material dragging and pile-up effects, and they appear later and larger for smaller n since the dragging effect is more significant for smaller n materials. After the maximum values, the deformation decreases as the sliding continues. When two asperities separate from each other, the plastic deformations remain at the final data points on each curve, which can be termed the vertical residual deformation. It can be found that the residual deformations are larger for smaller n cases.

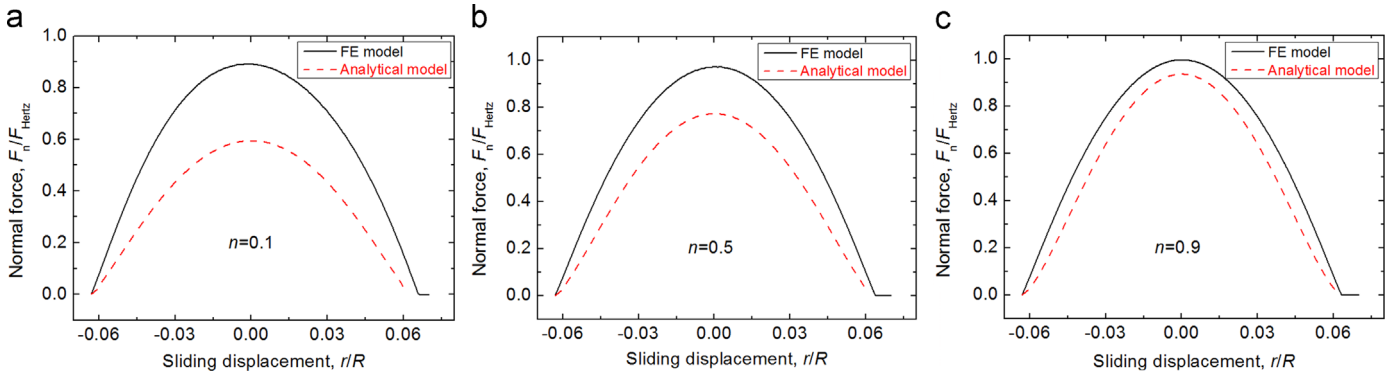

Fig. 3. The normal contact force in the sliding process at $\delta=0.001R$ obtained by the semi-analytical and FE models for materials with different hardening exponents n. (a) $n=0.1$, (b) $n=0.5$, (c) $n=0.9$.

Please cite this article as: B. Zhao, et al., Semi-analytical and numerical analysis of sliding asperity interaction for power-law hardening materials, Wear (2016), http://dx.doi.org/10.1016/j.wear.2016.07.010

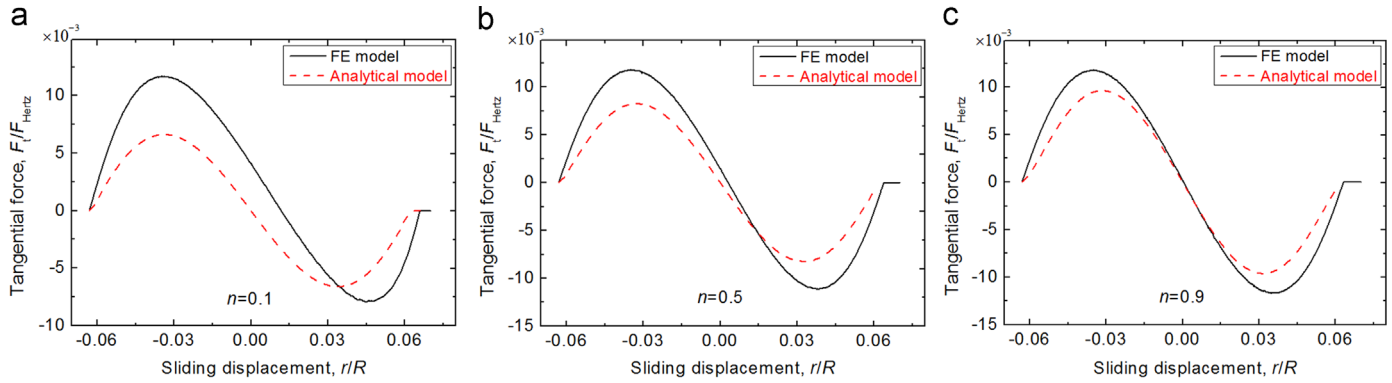

Fig. 4. The tangential contact force in the sliding process at $\delta=0.001R$ obtained by the semi-analytical and FE models for materials with different hardening exponents n. (a) $n=0.1$, (b) $n=0.5$, (c) $n=0.9$.

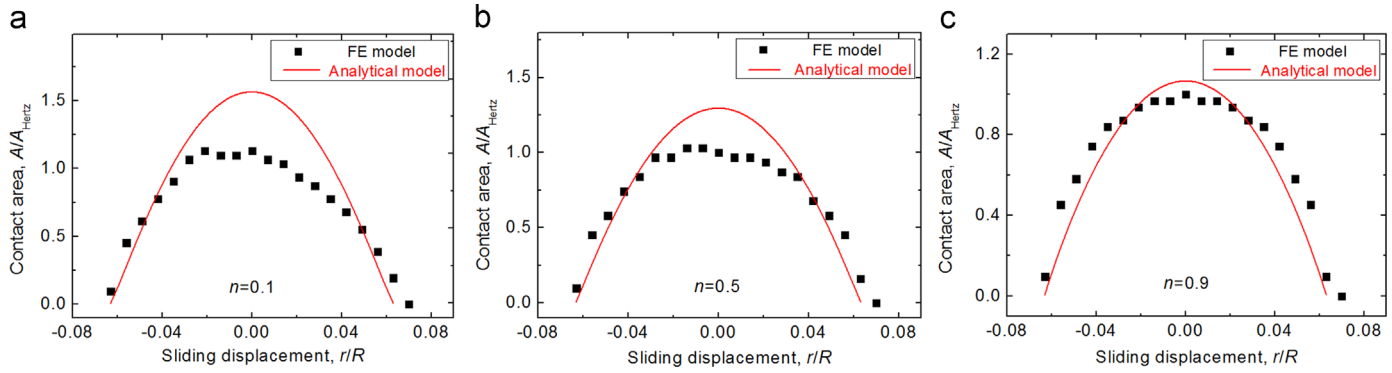

Fig. 5. The contact area in the sliding process at $\delta=0.001R$ obtained by the semi-analytical and FE models for materials with different hardening exponents n. (a) $n=0.1$, (b) $n=0.5$, (c) $n=0.9$.

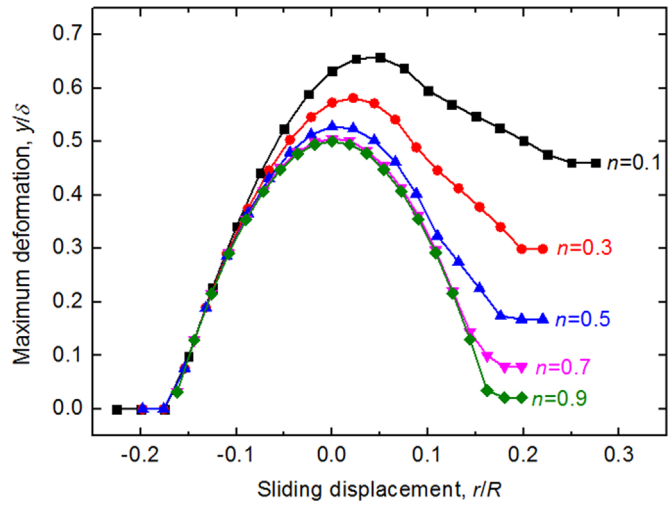

Fig. 6. The maximum vertical deformation in the Y direction, y, of the nodes on the profile of the upper asperity in the sliding process at $\delta=0.007R$ obtained by the FE model for materials with exponents n changing from 0.1 to 0.9.

Fig. 7 shows the real stress contours of the asperities of $n=0.3$ and 0.5 in the sliding process at three sliding displacements $r=-0.088R$, 0 (two in-contact cases) and $0.22R$ (after-contact case) at $\delta=0.007R$. It is clear in Fig. 7 that the stresses in these two asperities are anti-symmetric since they have the same material properties and geometries. When the asperities slide, smaller n materials result in larger stresses at the identical sliding displacement. In addition, the stresses show a tendency to move towards the leading edge along the sliding direction, which implies resistance to sliding. The trend is more significant for smaller n cases because the dragging and pile-up effects are more notable for the more plastic materials. Also because of shear dragging, it can be seen from the stress contours that when $r=0$, i.e. two asperities aligned vertically with respect to the axes of symmetry, the tangential forces could not be zero and will be shown in more detail later. When two asperities separate from each other after contact (e.g. $r=0.22R$ in Fig. 7), the stresses in each asperity are residual stresses, which are not symmetric. The regions of the residual stress at the trailing edge are larger than the leading edge due to the dragging effect, which is more noticeable for the smaller n cases.

Fig. 8 shows the contact area A, normalized by the Hertz results A_{Hertz}, for different exponents n at the overlap $\delta=0.005R$. It is clear that the contact areas are not symmetric for all cases, and all reach the maximum values before the sliding displacement $r=0$. The smaller n leads to the earlier and higher maximum contact area in the loading phase of the sliding, because in sliding, the material flattens and flows sideways since the material is being dragged and piled up. For more plastic materials, it is easier to flow plastically away from the contact surface, which causes the maximum contact area to occur earlier and to have a larger value.

Figs. 9 and 10 present the normal force F_n and the tangential force F_t in the sliding process which are normalized to the Hertz force F_{Hertz} for different n at $\delta=0.005R$, and show that both the normal and tangential forces are not symmetric. In Fig. 9, the curves of the normal forces in sliding are more skewed for large n materials, which is attributed to the more elastic resistance. The maximum normal forces appear before the vertical alignment axis ($r=0$), and for the smaller n cases, they occur earlier, but the values are smaller. In addition, the curves for smaller n cases go back to the zero later signifying that the two asperities separate from each other later, a result which also can be found for the tangential forces in Fig. 10, because of the more significant dragging effect. In Fig. 10, the positive maximum tangential forces also

Please cite this article as: B. Zhao, et al., Semi-analytical and numerical analysis of sliding asperity interaction for power-law hardening materials, Wear (2016), http://dx.doi.org/10.1016/j.wear.2016.07.010

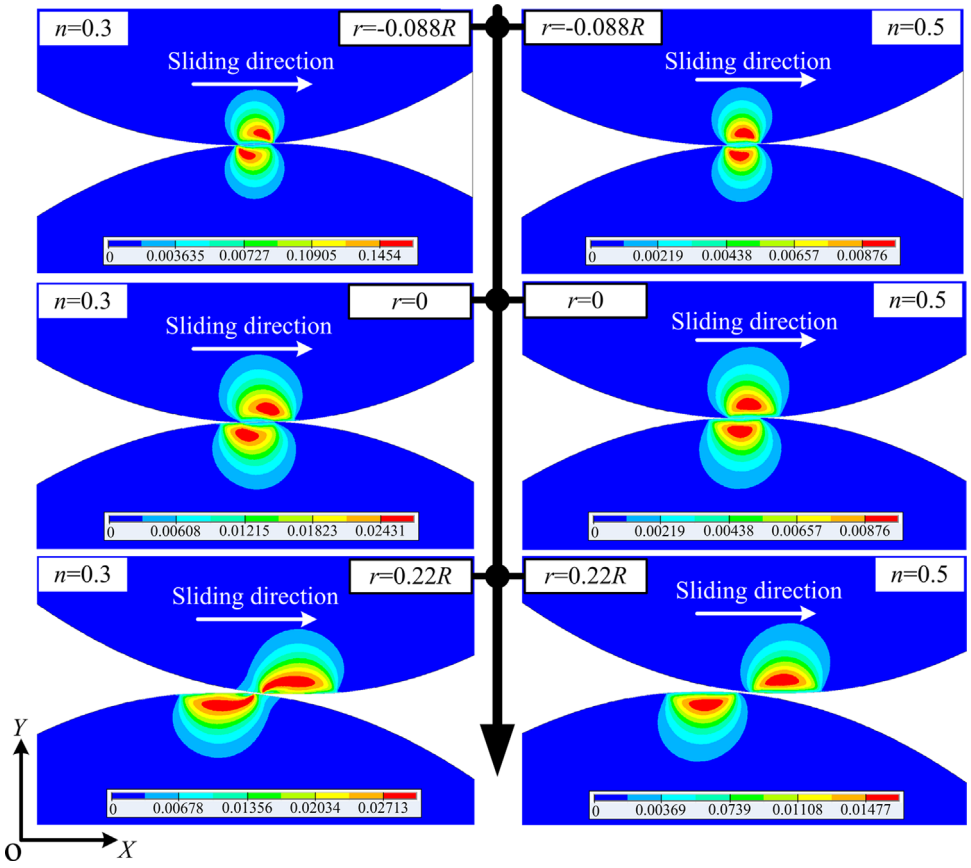

Fig. 7. The stress contours for sliding asperities whose hardening exponents $n=0.3$ and 0.5 at different sliding displacement $r=-0.088R$, 0 and $0.22R$ at $\delta=0.007R$.

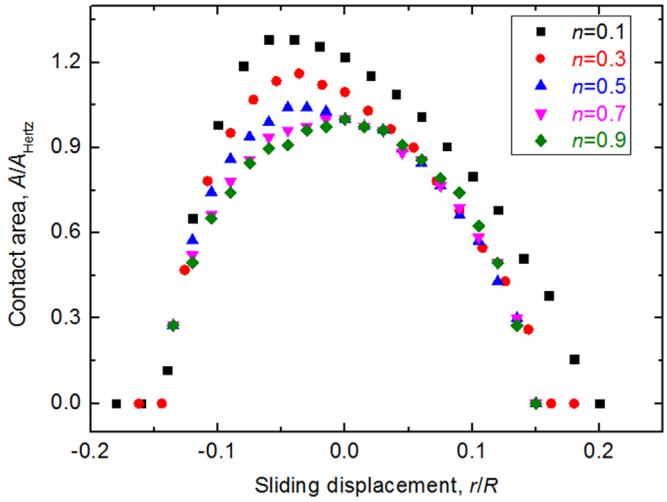

Fig. 8. The contact area in the sliding process at $\delta=0.005R$ for materials with hardening exponents n changing from 0.1 to 0.9.

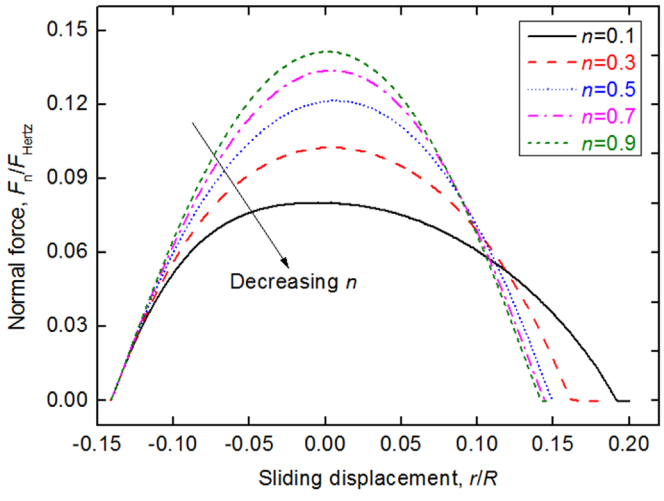

Fig. 9. The normal force in the sliding process at $\delta=0.005R$ for materials with hardening exponents n changing from 0.1 to 0.9.

appear earlier and are smaller when the exponent n is smaller. After reaching the maximum values, the tangential forces decrease. However, the tangential force will not return to zero at $r=0$ since permanent plastic deformation has occurred, which is also revealed by the stress contours in Fig. 7. For smaller n materials, the plastic deformation is larger, leading to a higher values at $r=0$ and lower negative maximum values in the subsequent sliding process.

Fig. 11 shows the energy loss U in the sliding process for different n at asperity overlaps $\delta=0.001R$, $0.003R$, $0.005R$ and $0.007R$, which are normalized by the critical elastic energy U_c. As the frictionless condition is adopted, the energy loss only comes from the material plasticity. The expression of U_c is given as follows [38]:

$$U_c=\frac{(\pi(1.33075+0.887825\nu+0.54373\nu^2)S_y)^5R^3}{60(E')^4} \tag{22}$$

where R is the radii of the summits of asperity. The energy loss is considered on the basis of the tangential force in Fig. 10, by calculating the difference of the area above the X axis (energy invested in sliding) and the area beneath the X axis (energy in the

Please cite this article as: B. Zhao, et al., Semi-analytical and numerical analysis of sliding asperity interaction for power-law hardening materials, Wear (2016), http://dx.doi.org/10.1016/j.wear.2016.07.010

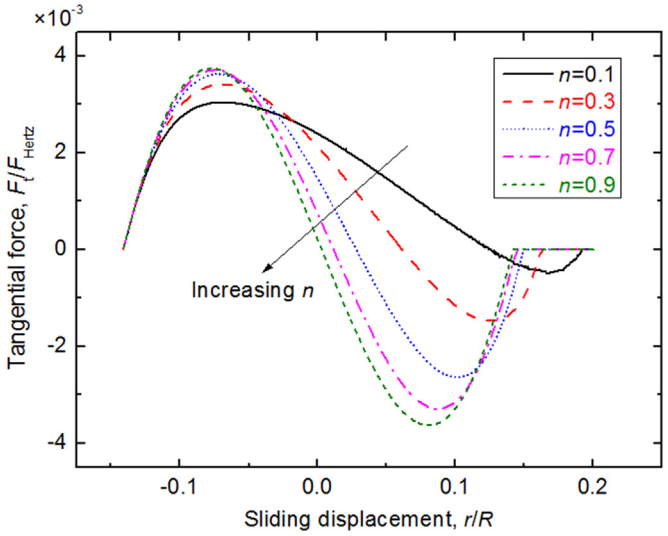

Fig. 10. The tangential force F_t in the sliding process at $\delta=0.005R$ for materials with hardening exponents n changing from 0.1 to 0.9.

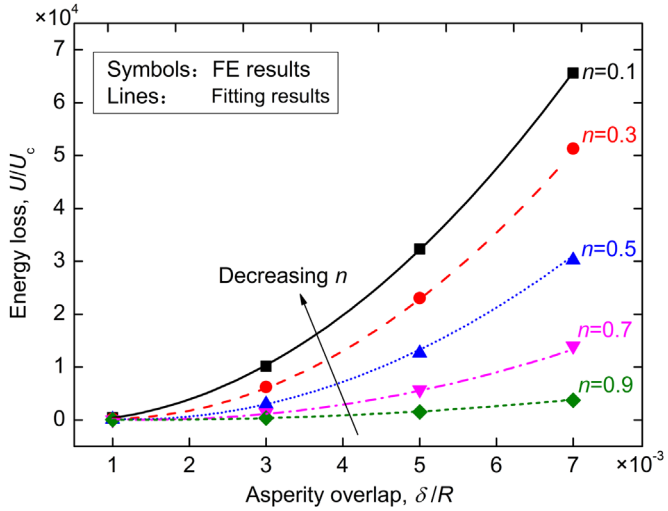

Fig. 11. The energy loss in the sliding process at asperity overlaps $\delta=0.001R$, $0.003R$, $0.005R$ and $0.007R$ for materials with hardening exponents n changing from 0.1 to 0.9.

rebound). It can be seen that as the overlap increases, the energy loss increases and more notably for smaller n materials. It should be noted that the values of the dimensionless energy loss U/U_c for different n at $\delta=0.001R$ ranging from 14.1 to 446.4, very close to 0 but not in fact. Furthermore, the energy loss for smaller n is larger for the same overlap due to more plastic deformation. The results given by the FE model can be fitted to the following equation:

$$U/U_c = m_1 + m_2(1000\delta/R) + m_3(1000\delta/R)^2 \tag{23}$$

where m_1, m_2 and m_3 are functions related to the hardening exponents n:

$$\begin{cases} m_1 = -1879 + 20440n - 35857.8n^2 + 17494.8n^3 \\ m_2 = 1041.9 - 24075.3n + 46654n^2 - 23978.6n^3 \\ m_3 = 1312.1 + 2562.8n - 9524n^2 + 5782n^3 \end{cases}. \tag{24}$$

Actually, friction plays an important role in the real sliding process, and its effect due to contact friction and local plasticity are expected to be very significant especially under relatively large asperity overlaps. Ignoring friction physically speaking is not valid.

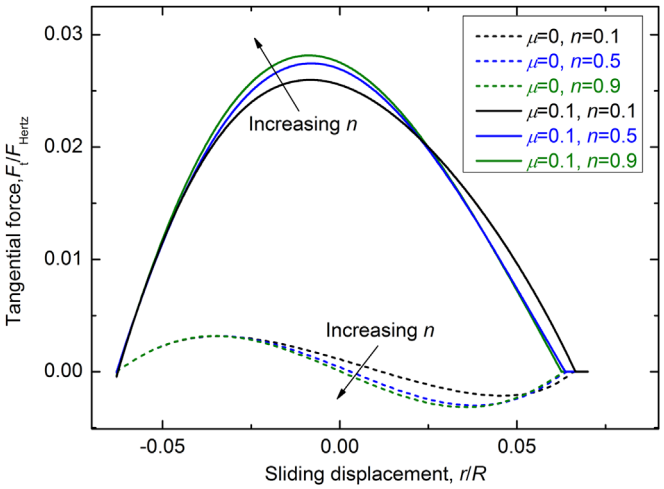

Fig. 12. The tangential force F_t in the aforementioned frictionless ($\mu=0$) and frictional ($\mu=0.1$) sliding process at $\delta=0.001R$ for $n=0.1$, 0.5 and 0.9.

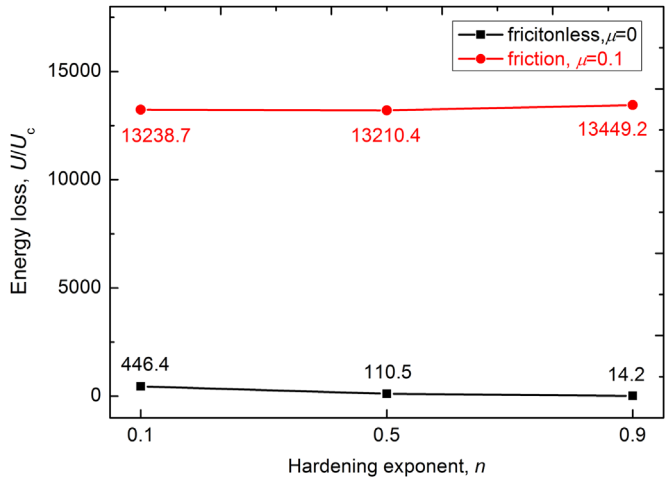

Fig. 13. The energy loss in the aforementioned frictionless ($\mu=0$) and frictional ($\mu=0.1$) sliding process at asperity overlaps $\delta=0.001R$ for $n=0.1$, 0.5 and 0.9.

Therefore, the sliding process under the frictional condition is preliminarily analyzed next with the FE model, and is compared with the aforementioned frictionless cases. The coefficient of friction μ is set as 0.1, which is the only difference from the frictionless FE model. The cases at the asperity overlap $\delta=0.001R$ are considered, and the tangential force F_t normalized to the Hertz force F_{Hertz} is shown in Fig. 12. It can be seen from Fig. 12 that all the curves plotted for the frictional sliding process show positive values, which is not similar to the frictionless curves. For the frictional cases, the values of F_t are much larger than those for the frictionless cases, and the maximum values appear before the vertical alignment axis ($r=0$). For the materials with larger n, the maximum values of F_t is larger and the curves go back to zero earlier than the smaller n materials. In the frictional sliding process, the area under the tangential force curve is much larger than that in the frictionless sliding process, which reveals the friction causes much larger energy loss as shown in Fig. 13. It is expected that the energy loss in the frictionless sliding process is purely due to the plastic deformation; while in the frictional sliding process, the energy loss is attributed to both the local plasticity and the friction, and the part caused by the friction is significantly large. This is just a preliminary consideration about the frictional sliding process, which gives some inspiration about the effect of the friction. A more detail study is still needed, which will be considered in the future.

Please cite this article as: B. Zhao, et al., Semi-analytical and numerical analysis of sliding asperity interaction for power-law hardening materials, Wear (2016), http://dx.doi.org/10.1016/j.wear.2016.07.010

5. Conclusions

To study the sliding interaction between asperities whose profiles were approximated as parabolas for power-law hardening materials, both a semi-analytical model and a numerical model were developed. The semi-analytical model regarded the sliding process as consisting of many loading and unloading processes, and the effect of the plastic deformation with the residual deformation were considered. The results obtained from these two models were compared, and in addition, the effect of the strain hardening exponents on the contact parameters was investigated using the FE model. Two main conclusions were obtained:

(1) The semi-analytical model was much faster than the FE model to solve the same sliding problem, but it could only be applied for those cases where the interferences were in an appropriate range ($0 < w_1/w_c < 110$). The semi-analytical results agreed well with the FE model for the materials with larger n, while for the smaller n cases, the larger errors would preclude its use. Since the hardening exponents for many realistic materials are relative small or moderate, the applicability of the semi-analytical solution developed for realistic situations needs further improvement. However, the semi-analytical model might give some helpful insights that the sliding process could be explored from empirical expressions.
(2) As the exponents n decreased, the dragging effect was more notable, leading to a more significant influence on the contact parameters. For smaller n cases, the vertical displacement in sliding and the residual deformation after sliding were both larger, and the stresses also became larger and moved more towards the leading edge along the sliding direction. The contact area and energy loss increased, while the maximum values of the normal and tangential forces decreased with the decrease of n. Friction significantly affects the contact parameters in the sliding process, enlarging the tangential forces and energy loss, which should be considered in detail further.

Acknowledgment

This work was supported by Independent Innovation Project of Shandong Province (Grant no. 2014ZZCX04101) and the scholarship from China Scholarship Council (Grant no. 201506220077).

References

[1] M. Fellah, M.A. Samad, M. Labaiz, O. Assala, A. Iost, Sliding friction and wear performance of the nano-bioceramic α-Al_2O_3prepared by high energy milling, Tribol. Int. 91 (2015) 151–159.
[2] G. Hammes, R. Schroeder, C. Binder, A.N. Klein, J.D.B. de Mello, Effect of double pressing/double sintering on the sliding wear of self-lubricating sintered composites, Tribol. Int. 70 (2014) 119–127.
[3] B.P. Chang, H.M. Akil, R.B.M. Nasir, Comparative study of micro-and nano-ZnO reinforced UHMWPE composites under dry sliding wear, Wear 297 (1) (2013) 1120–1127.
[4] Y. Birol, Sliding wear of CrN, AlCrN and AlTiN coated AISI H13 hot work tool steels in aluminium extrusion, Tribol. Int. 57 (2013) 101–106.
[5] L. Ceschini, C. Chiavari, A. Marconi, C. Martini, Influence of the countermaterial on the dry sliding friction and wear behaviour of low temperature carburized AISI316L steel, Tribol. Int. 67 (2013) 36–43.
[6] M. Lieblich, J. Corrochano, J. Ibáñez, V. Vadillo, J.C. Walker, W.M. Rainforth, Subsurface modifications in powder metallurgy aluminium alloy composites reinforced with intermetallic $MoSi_2$ particles under dry sliding wear, Wear 309 (1) (2014) 126–133.
[7] L. Tang, C. Gao, J. Huang, H. Zhang, W. Chang, Dry sliding friction and wear behaviour of hardened AISI D2 tool steel with different hardness levels, Tribol. Int .66 (2013) 165–173.
[8] Y. Sun, Sliding wear behaviour of surface mechanical attrition treated AISI 304 stainless steel, Tribol. Int. 57 (2013) 67–75.
[9] T.R. Prabhu, V.K. Varma, S. Vedantam, Effect of SiC volume fraction and size on dry sliding wear of Fe/SiC/graphite hybrid composites for high sliding speed applications, Wear 309 (1) (2014) 1–10.
[10] K.L. Johnson, K.L. Johnson, Contact Mechanics, Cambridge university press, 1987.
[11] J.A. Greenwood, J.B.P. Williamson, Contact of nominally flat surfaces, Proc. R. Soc. A: Math. Phys. Eng. Sci. 295 (1442) (1966) 300–319.
[12] J. Greenwood, J. Tripp, The contact of two nominally flat rough surfaces, Proc. Inst. Mech. Eng. 185 (1) (1970) 625–633.
[13] W.R. Chang, I. Etsion, D.B. Bogy, An elastic–plastic model for the contact of rough surfaces, J. Tribol. 109 (2) (1987) 257–263.
[14] L. Kogut, I. Etsion, Elastic–plastic contact analysis of a sphere and a rigid flat, J. Appl. Mech. 69 (5) (2002) 657.
[15] R.L. Jackson, I. Green, A finite element study of elasto-plastic hemispherical contact against a rigid flat, J. Tribol. 127 (2) (2005) 343.
[16] I. Etsion, Y. Kligerman, Y. Kadin, Unloading of an elastic–plastic loaded spherical contact, Int. J. Solids Struct. 42 (13) (2005) 3716–3729.
[17] J.H. Zhao, S. Nagao, Z.L. Zhang, Loading and unloading of a spherical contact: from elastic to elastic–perfectly plastic materials, Int. J. Mech. Sci. 56 (1) (2012) 70–76.
[18] G. Hamilton, L. Goodman, The stress field created by a circular sliding contact, J. Appl. Mech. 33 (2) (1966) 371–376.
[19] G.M. Hamilton, Explicit equations for the stresses beneath a sliding spherical contact, Proc. Inst. Mech. Eng. Part C: J. Mech. Eng. Sci. 197 (1) (1983) 53–59.
[20] A. Tangena, P. Wijnhoven, Finite element calculations on the influence of surface roughness on friction, Wear 103 (4) (1985) 345–354.
[21] A. Faulkner, R. Arnell, The development of a finite element model to simulate the sliding interaction between two, three-dimensional, elastoplastic, hemispherical asperities, Wear 242 (1) (2000) 114–122.
[22] R. Vijaywargiya, I. Green, A finite element study of the deformations, forces, stress formations, and energy losses in sliding cylindrical contacts, Int. J. Non-Linear Mech. 42 (7) (2007) 914–927.
[23] R.L. Jackson, R.S. Duvvuru, H. Meghani, M. Mahajan, An analysis of elasto-plastic sliding spherical asperity interaction, Wear 262 (1-2) (2007) 210–219.
[24] D.M. Mulvihill, M.E. Kartal, D. Nowell, D.A. Hills, An elastic–plastic asperity interaction model for sliding friction, Tribol. Int. 44 (12) (2011) 1679–1694.
[25] J.J. Dawkins, R.W. Neu, Influence of crystallographic orientation on energy dissipation during sliding, J. Tribol. 130 (4) (2008) 041604.
[26] N.A. Fleck, G.M. Muller, M.F. Ashby, et al., Strain gradient plasticity: theory and experiment, Acta Metall. Mater. 42 (2) (1994) 475–487.
[27] A. Ovcharenko, G. Halperin, I. Etsion, Experimental study of adhesive static friction in a spherical elastic–plastic contact, , 130 (2) (2008) 021401.
[28] A. Ovcharenko, G. Halperin, I. Etsion, In situ and real-time optical investigation of junction growth in spherical elastic–plastic contact, Wear 264 (11) (2008) 1043–1050.
[29] P. Prokopovich, S. Perni, Multiasperity contact adhesion model for universal asperity height and radius of curvature distributions, Langmuir 26 (22) (2010) 17028–17036.
[30] A. Sepehri, K. Farhang, On elastic interaction of nominally flat rough surfaces, J. Tribol. 130 (1) (2008) 011014.
[31] R. Jackson, I. Chusoipin, I. Green, A finite element study of the residual stress and deformation in hemispherical contacts, J. Tribol. 127 (3) (2005) 484.
[32] L. Kogut, I. Etsion, A semi-analytical solution for the sliding inception of a spherical contact, J. Tribol. 125 (3) (2003) 499.
[33] W. Ramberg, W.R. Osgood, Description of stress–strain curves by three parameters, NACA (Technical Note) 902 (1943) 1–28.
[34] B. Zhao, S. Zhang, P. Wang, Y. Hai, Loading–unloading normal stiffness model for power-law hardening surfaces considering actual surface topography, Tribol. Int. 90 (2015) 332–342.
[35] A. Sepehri, K. Farhang, Closed-form equations for contact force and moment in elastic contact of rough surfaces, Modell. Simul. Eng. 2011 (2011) 1–14.
[36] V. Brizmer, Y. Kligerman, I. Etsion, Elastic–plastic spherical contact under combined normal and tangential loading in full stick, Tribol. Lett. 25 (1) (2006) 61–70.
[37] A. Wu, X. Shi, A.A. Polycarpou, An elastic–plastic spherical contact model under combined normal and tangential loading, J. Appl. Mech. 79 (5) (2012) 051001.
[38] I. Green, Poisson ratio effects and critical values in spherical and cylindrical Hertzian contacts, Appl. Mech. Eng. 10 (3) (2005) 451.

Please cite this article as: B. Zhao, et al., Semi-analytical and numerical analysis of sliding asperity interaction for power-law hardening materials, Wear (2016), http://dx.doi.org/10.1016/j.wear.2016.07.010